

# Exploiting seismic signal and noise in an intracratonic environment to constrain crustal structure and source parameters of infrequent earthquakes

Mallory K. Young,<sup>1</sup> Hrvoje Tkalčić,<sup>1</sup> Nicholas Rawlinson<sup>1</sup> and Anya M. Reading<sup>2</sup>

<sup>1</sup>Research School of Earth Sciences, The Australian National University, Mills Road, Building 61, Canberra, ACT 0200, Australia.

E-mail: mallory.young@anu.edu.au

<sup>2</sup>School of Earth Sciences, The University of Tasmania, Private Bag 79, TAS 7001, Australia

Accepted 2011 November 30. Received 2011 November 30; in original form 2011 May 6

## SUMMARY

In many regions of the world characterized by a relatively low rate of seismicity, the determination of local and regional seismic source parameters is often restricted to an analysis of the first onsets of *P* waves (or first motion analysis) due to incomplete information about Earth structure and the small size of the events. When rare large earthquakes occur in these regions, their waveforms can be used to model Earth structure. This, however, makes the nature of the earthquake source determination problem circular, as source information is mapped as structure. Presented here is one possible remedy to this situation, where through a two-step approach we first constrain Earth structure using data independent of the earthquake of interest. In this study, we focus on a region in Western Australia with low seismicity and minimal instrument coverage and use the CAPRA/LP temporary deployment to demonstrate that reliable structural models of the upper lithosphere can be obtained from an independent collection of teleseismic and ambient noise datasets. Apart from teleseismic receiver functions (RFs), we obtain group velocities from the cross-correlation of ambient noise and phase velocities from the traditional two-station method using carefully selected teleseismic earthquakes and station pairs. Crustal models are then developed through the joint inversion of dispersion data and RFs, and structural Green's functions are computed from a layered composite model. In the second step of this comprehensive approach, we apply full waveform inversion (three-component body and surface waves) to the 2007  $M_L = 5.3$  Shark Bay, Western Australia, earthquake to estimate its source parameters (seismic moment, focal mechanism, and depth). We conclude that the full waveform inversion analysis provides constraints on the orientation of fault planes superior to a first motion interpretation.

**Key words:** Composition of the continental crust; Earthquake source observations; Body waves; Seismic tomography; Australia.

## 1 INTRODUCTION

### 1.1 Motivation

On 2007 February 15 Western Australia (WA) experienced a rare magnitude 5.3 earthquake approximately 18 km beneath Shark Bay [Figs 1(a) and (b)]. Its location ( $-25.97^\circ$  N,  $113.28^\circ$  E, 18 km depth), origin time (UTC: 15:38:36), and size ( $M_L = 5.3$ ) were determined by Geoscience Australia (GA), which uses a network of permanent broad-band seismometers operating in real-time ([www.ga.gov.au](http://www.ga.gov.au)). Although Australia is generally seismically quiet, one magnitude 6.0 event occurs approximately every five years (e.g. McCue 1990). Careful analysis of these anomalous events is necessary to establish a model for describing the causes, character, and frequency of

intraplate earthquakes (e.g. Stein 2007) as well as the state of the regional stress-field (e.g. Clark & Leonard 2003).

In order to invert a seismic waveform for source properties, the structure of the Earth between the source and receiver must be understood (Aki & Richards 2002). Unfortunately, mapping the Earth's crust is not an easy task in a seismically inactive region sparsely covered by recording stations. Under these circumstances, simpler and structure-independent methods of determining seismic moment tensors are often employed. The most straightforward approach is to evaluate the polarity of *P*-wave first motions recorded by seismic stations that provide adequate azimuthal coverage of the source. *S*- and *P*-wave amplitude ratios have also been utilized with success to constrain focal mechanisms (e.g. Julian & Foulger 1996; Julian *et al.* 1997; Hardebeck & Shearer 2003). The solutions, however,

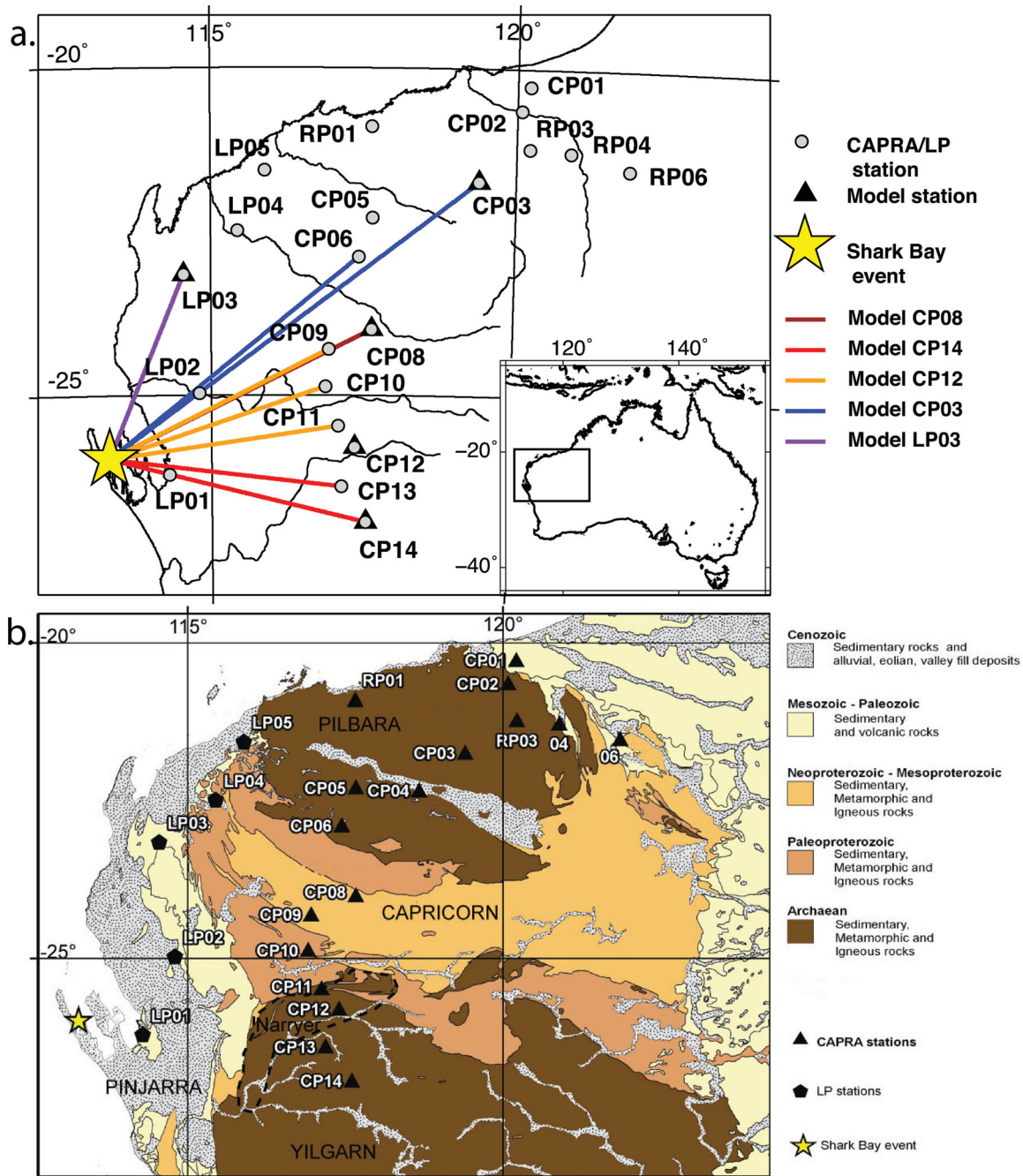


**Figure 1.** (a) Location of all CAPRA/LP stations used in this study along with the epicentre of the 2007 February Shark Bay event (marked by the yellow star). ‘Model stations’ refer to stations for which a 1-D Earth model of the crust and upper lithosphere is created using a joint inversion of receiver functions and dispersion information. Stations with names beginning with ‘CP’ and ‘RP’ are part of the CAPRA array deployed by the Australian National University. Stations with names beginning with ‘LP’ were deployed by the University of Western Australia. Coloured lines between source and receiver indicate the model used for each station. (b) Tectonic elements of Western Australia.

depend on the clarity of phase arrivals and the position of stations with relation to epicentral distance and azimuthal distribution.

Reverts *et al.* (2009) calculated the focal mechanism of the Shark Bay event from first motion *P*-wave data alone. They used mainly temporary stations, positioned east of the source, that were deployed at the time of the Shark Bay earthquake. The combination of limited azimuthal station coverage and the rather emergent character of the recorded waveforms suggests that constraints on the source parameters of the Shark Bay event could be improved by further, more detailed analysis. A combined interpretation of full waveform

inversion and first motion solutions can provide a more robust conclusion, and this approach may become more widely employed. Such an approach requires a careful, initial determination of Earth structure in the region, which is outlined in the following section.

### 1.2 A two-step approach

When rare significant earthquakes like the Shark Bay event occur in relatively low seismicity regions such as WA, their waveforms

provide invaluable data with which to model Earth structure. However, it is also advisable that Earth structure be constrained using independent datasets in order to minimize any mapping of source information as structure. In this case, such data is limited to either small local events weakly recorded at several GA stations located far from Shark Bay, or, preferably, teleseismic events recorded during a temporary deployment located closer to Shark Bay. In addition, ambient noise Earth imaging techniques improve knowledge of the seismic wavespeeds in the upper crust and, therefore, can be invaluable when seismicity is sparse.

The CAPRA deployment, consisting of 22 three-component broad-band stations installed in WA by the Research School of Earth Sciences at the Australian National University (Reading *et al.* 2011) with the goal of studying deep structure, was operational at the time of the Shark Bay event. The presence of these stations enables us to produce a working composite model of WA that reflects the different Moho character and seismic velocities of each geological region.

The ancient West Australia Craton was assembled as a result of the collision of the Archaean Pilbara and Yilgarn cratons. They were joined along the Capricorn Orogen with the Pinjarra Orogen bounding them to the west (Fitzsimons 2003). Forward modelling is used to create initial crustal models of these regions that are fed into a linearized joint inversion of teleseismic receiver functions (RFs) and group and phase dispersion curves calculated from a combination of teleseismic signals and ambient noise data.

This procedure is naturally divided into two steps: in the first step, we determine Earth structure within the region spanned by the source and receiver array using a multiplicity of methods, and in the second step, we use this information to invert for the seismic moment tensor of the Shark Bay earthquake. We are able to invert the long period waveforms (15–35 s) recorded at CAPRA/LP stations within approximately 750 km of the epicentre to produce a seismic moment tensor and depth estimate for the Shark Bay event. In addition, we perform our own first motion analysis and provide an appraisal of this method in the light of previous work.

## 2 TECTONIC SETTING

The following tectonic elements are crossed by energy from the Shark Bay earthquake to the recording stations used in this study: Pilbara Craton, Yilgarn Craton, Capricorn Orogen, and Pinjarra Orogen (Fig. 1b). The Pilbara Craton in northwest WA comprises a granite-greenstone terrain of early mid Archaean age (Wellman 2000). The east and west Pilbara Craton are geologically disparate from one another and evolved under two different tectonic regimes (Hickman 2004). The East Pilbara Terrane contains randomly orientated dome and basin structures that alternate with synclinal greenstone (volcano-sedimentary rocks) belts (Van Kranendonk *et al.* 2007). This dome and basin pattern is absent in the West Pilbara Terrane, which is instead dominated by elongated granitoid complexes, greenstone belts, and numerous east and northeast striking faults (Hickman 2004). The Yilgarn Craton, in southwest Australia, formed during a Proterozoic episode of increased tectonic activity that resulted in the amalgamation of various continental fragments (Cassidy *et al.* 2006). Granite and greenstones form the majority of the upper crust, and deeper Late Archaean crustal layers are exposed in the northwest and southwest (Ivanić *et al.* 2010). At the northwest corner of the Yilgarn Craton lies the Narryer Terrane, which contains the oldest crust in Australia (Spaggiari *et al.* 2008).

The joining of the Pilbara and Yilgarn Cratons in the Palaeo-

proterozoic produced the 300 km wide, heavily deformed, tectonic belt known as the Capricorn Orogen (Tyler & Thorne 1990; Betts *et al.* 2002; Sheppard *et al.* 2010). The orogen contains Palaeoproterozoic plutonic igneous rocks, medium- to high-grade metamorphic rocks, a series of volcano-sedimentary and sedimentary basins, and is rimmed by the deformed margins of the Pilbara and Yilgarn cratons (Cawood & Tyler 2004). To the west of the Darling Fault lies the Neoproterozoic Pinjarra Orogen, which is the resulting passive margin that formed when Australia separated from India (Myers *et al.* 1996). The rift valley is concealed by 10–15 km of sedimentary rocks, and so little of its Precambrian geological history is known. Some evidence is, however, provided by three main sources of exposed Precambrian rocks in the Leeuwin, Mullingarra, and Northampton complexes (Myers 1993).

Previous seismic studies in this part of WA have utilised RF, reflection and refraction data. Drummond (1988) used reflection and refractions studies to characterize the Pilbara and Yilgarn Cratons as having a two-layered crust with a broad transition between these layers occurring between 10 and 15 km depth. He estimated the Moho to lie between 28 and 35 km depth. Clitheroe *et al.* (2000) inverted RFs for shear velocity profiles beneath 65 broad-band stations across Australia and combined the results with 51 independent estimates of crustal thickness from refraction and reflection profiles to produce a Moho map of the continent. He found the crust to be thin and the Moho transition to be sharp beneath the Archaean cratons. A few years later, Collins *et al.* (2003) confirmed the results of Clitheroe *et al.* (2000) using additional data newly acquired from refraction and reflection profiles. Using mostly temporary seismic stations, Reading & Kennett (2003) completed a RF analysis of the Pilbara Craton, Capricorn Orogen, and northern Yilgarn Craton. They characterised the Pilbara Craton as having a sharp, shallow (~30 km) Moho, the Yilgarn as having a sharp, yet deeper (~40 km) Moho, and were barely able to discern the Moho beneath the Capricorn Orogen. Reading *et al.* (2011) provide a more comprehensive analysis of the Moho character of the region using RFs from the CAPRA deployment. In general, they found a deeper Moho transition (36–44 km depth) beneath the Capricorn Orogen; a sharper, less deep (~35 km) Moho in the north Yilgarn Craton, except for the Narryer terrane, which exhibits an abnormally shallow discontinuity at 29 km; and a shallower (29–34 km), more pronounced discontinuity beneath the Pilbara Craton.

We will use data from stations CP08, CP09, CP10, and CP11 to constrain the structure within the Capricorn Orogen; stations CP14 and CP13 for the Yilgarn Craton, with CP12 on the Narryer Terrane; and stations CP02, CP03, CP05, CP06, RP01, RP03, and RP04 for the Pilbara Craton (Fig. 1b). There have been no previous RF analyses of the Pinjarra Orogen, but we expect to find a thinner crust (Clitheroe *et al.* 2000; Collins *et al.* 2003) relative to the cratons and a thin surface layer of sediments using stations LP01, LP02, LP03, LP04, and LP05 (Fig. 1b).

## 3 DATA AND METHODS

In this study, we use data recorded at a total of 17 CAPRA seismic stations. There were two main transects recording between 2006 June and 2007 June: one running roughly north-south (Table 1; CP stations in Figs 1(a) and (b)), and another running west-east along the Telfer Road [Table 1; RP stations in Figs 1(a) and (b)]. Data from five stations operated by the University of Western Australia were also incorporated [Table 1; LP stations in Figs 1(a) and (b)]. This transect ran along the northwestern margin of WA between 2005

**Table 1.** All CAPRA and LP stations used in the development of the 1-D composite model along with respective geographical coordinates. An 'x' indicates that that station was used for a particular analysis method as indicated by the respective column headings.

Station Name	Latitude (°)	Longitude (°)	Receiver Function Analysis	Ambient Noise Analysis	Two-Station Method	First Motion Analysis	Final Composite Model	Moment Tensor Inversion
CP14	-26.93	117.60	x	x	x	x	x	x
CP13	-26.39	117.18		x		x		x
CP12	-25.79	117.40	x	x		x	x	
CP11	-25.47	117.12		x		x		x
CP10	-24.86	116.91		x		x		x
CP09	-24.29	116.96		x		x		x
CP08	-23.99	117.67	x	x	x	x	x	x
CP06	-22.88	117.44		x				x
CP05	-22.28	117.67		x		x		
CP04	-22.33	118.67		x				
CP03	-21.73	119.40	x	x	x	x	x	x
CP02	-20.63	120.08		x		x		
CP01	-20.26	120.21		x		x		
RP01	-20.89	117.64		x		x		
RP03	-21.22	120.22		x		x		
RP04	-21.27	120.89		x		x		
RP06	-21.51	121.85		x		x		
LP01	-26.21	114.29	x	x	x			
LP02	-24.96	114.80		x				
LP03	-23.15	114.55	x	x	x	x	x	x
LP04	-22.49	115.45		x		x		
LP05	-21.56	115.89		x		x		

October and 2007 April. The CP and RP stations consisted of Earth-Data recorders and Guralp CMG-3ESP sensors (with the exception of CP13 where a Streckeissen STS-2 was deployed) while the LP stations had Reftek recorders and CMG-40T sensors. Five representative models produced for the region are entitled CP14, CP12, CP08, CP03, and LP03 (Fig. 1a). These models together represent a composite model that is used to produce synthetic waveforms for the seismic moment tensor inversion. In the following sections, we will describe three methods that were applied to the CAPRA/LP data to obtain this composite 1-D model of the Earth. In the last part of each of the following subsections, we state the results of the structure determination (step 1), which are subsequently used in the complete waveform inversion for an improved focal mechanism (step 2).

### 3.1 Receiver function analysis

RF analysis is a popular method for determining a shear-wave model of the lithosphere beneath a station. By deconvolving the vertical with the radial response of a plane-layered structure, the shear-wave response of the crust and upper mantle can be extracted to produce a time series called a RF (Langston 1979). RFs are particularly sensitive to pronounced gradients in elastic properties as a function of depth and are critical to determining the depth of the Moho.

In this study, RFs are calculated from teleseismic events using a relatively conservative threshold on earthquake magnitudes of 5.0 or greater. The events, mainly from surrounding subduction zones of Indonesia, Japan, and Tonga-Fiji (Fig. 2), are pre-processed, and only coherent waveforms are selected for further analysis. The waveforms are iteratively deconvolved in the time domain according to Ligorria & Ammon (1999) using a 2.5 Gaussian filter. The resulting RFs are subsequently band-pass filtered to decrease the noise and improve coherency using an optimised filter width: band-pass

between 0.75 Hz and 2.0 Hz for stations CP14 and CP12, bandpass between 1.0 Hz and 2.5 Hz for stations CP08 and CP03, and a high-pass with a corner frequency of 0.4 Hz for stations LP01 and LP03. RFs for a back-azimuth range of approximately 20° are selected and stacked for each station to create an average RF which is used in the linearised inversion.

The first step in inverting RFs for a 1-D model is to produce a reasonable initial model, as the final solution will not be allowed to differ greatly from the initial model. We utilize *a priori* information from previous studies (Reading & Kennett 2003) in our forward modelling approach using the RF forward modelling software IRFFM (Tkalčić *et al.* 2011a). This interactive tool allows manual manipulation of thicknesses, velocities, and  $v_p/v_s$  ratios for a 1-D Earth model. A simple model with two crustal layers is created to represent the Earth's structure beneath each of the following six stations: CP14, CP12, CP08, CP03, LP03, and LP01 (Table 1). These become the initial models in a linearised inversion (Julia *et al.* 2000) that allows easy manipulation of the smoothness parameter. We find an inverted shear velocity model that produces synthetic RFs with a high variance reduction (VR) by taking the initial model and iteratively perturbing each layer. Increasing the number of layers in a model improves the fit between the observed and synthetic RF at the expense of over-parametrizing the model space. Likewise, increasing the smoothness parameter makes a model more realistic at the expense of decreasing the data fit. Through a grid-search, the number of layers and the smoothness parameter are systematically varied for each model. In this manner we are able to explore the VR achieved throughout the entire parameter space and estimate the optimal number of layers in our models. For each model, the number of layers is increased until further layers produce no significant improvement in VR (Tkalčić *et al.* 2011a). A collection of models for each station consists of versions with a different number of layers, smoothness parameter, and iteration numbers, all of which are empirically determined. The preferred model is an

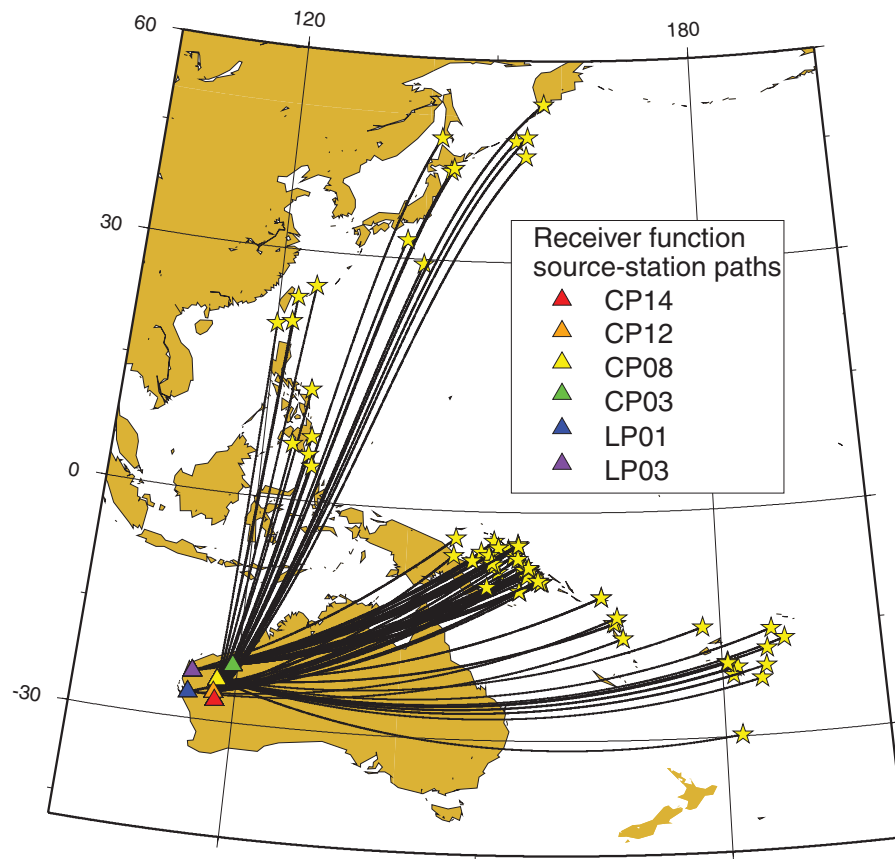


**Figure 2.** Map showing all source-receiver pairs used in the receiver function analysis. Sources are marked by yellow stars and stations by coloured triangles.

average over a limited range of these models. For example, the final CP14 model is averaged over versions having seven or nine crustal layers, smoothnesses of 0.2 or 0.3, and iterations between 10 and 40. The models are divided into 1 km thick layers to facilitate the averaging of models with different numbers of velocity discontinuities. Though the resulting final averaged model does not have the overall best fit, it provides a more probable representation of the Earth's structure beneath a given station.

Fig. 6(a) provides the final model as inverted from the RF data for CP14 (light blue dashed line). Located near the northern rim of the Yilgarn Craton, the interpreted Moho depth of CP14 is approximately 34 km, which is in good agreement with previous RF studies (Clitheroe *et al.* 2000; Collins *et al.* 2003; Reading & Kennett 2003; Reading *et al.* 2011). The RFs of CP12 in general have an ill-defined and inconsistent peak around 3.5 s, yielding less obvious information about the character of the Moho, but the beginning of a broad transition is seen at about 28 km (Fig. 6b). Reading *et al.* (2011) infer a sharp transition at CP12 at this depth (although not a very large seismic velocity contrast), which is likely due to the slight difference between the two inversion methods. The Moho of station CP08 appears to begin at around 30 km depth, and, consistent with the work of Reading *et al.* (2011), there is an upper crustal discontinuity at around 8 km depth (Fig. 6c). CP03 has a distinct Moho transition around 28 km (Fig. 6d). The RFs of both LP01 and LP03 are very noisy, and thus the majority of them are discarded from the final stacking. Nonetheless, the average RF for LP03 does show a strong arrival at around 4 s. Upon inversion, a strong low velocity zone in the uppermost 4 km of crust – probably due to coastal sediments – and a Moho transition at 31 km result (Fig. 6e). LP01 lacks a sharp Moho; a gradual transition begins at

about 27 km depth, and a lower velocity layer in the upper crust is present as with LP03. Although a detailed RF assessment of the Pinjarra region has not yet been completed, these values are in good agreement with the rough estimates for the region given by Collins *et al.* (2003) in his analysis of the crustal thickness of Australia.

### 3.2 Surface wave dispersion curves

#### 3.2.1 Group velocity from ambient noise

Although RFs provide good estimates of velocity contrasts, when combined with dispersion data, they more accurately and uniquely predict the average velocities in the crust (e.g. Özalaybey *et al.* 1997; Du & Foulger 1999; Julia *et al.* 2000; Tkalčić *et al.* 2006; Tkalčić *et al.* 2011b). In this study, we calculate Rayleigh wave Green's functions for the Earth between all possible stations pairs through the cross-correlation of ambient noise recorded by the CAPRA/LP array (Table 1). The Green's functions reveal short-period velocity information important for resolving crustal and upper mantle structure. An automated frequency-time analysis (FTAN) procedure according to Bensen *et al.* (2007) is followed along with the few modifications described by Arroucau *et al.* (2010) as a means of measuring group velocities. Cross-correlations of 40-minute noise segments (with 75 per cent overlap) recorded by all possible station pairs are stacked over a period of nine months starting on 2006 July 1. The negative time derivative of the symmetric component of the resulting average cross-correlograms provides an estimate of the Rayleigh wave Green's functions between each station pair within a frequency-dependent amplitude factor (Lobkis & Weaver

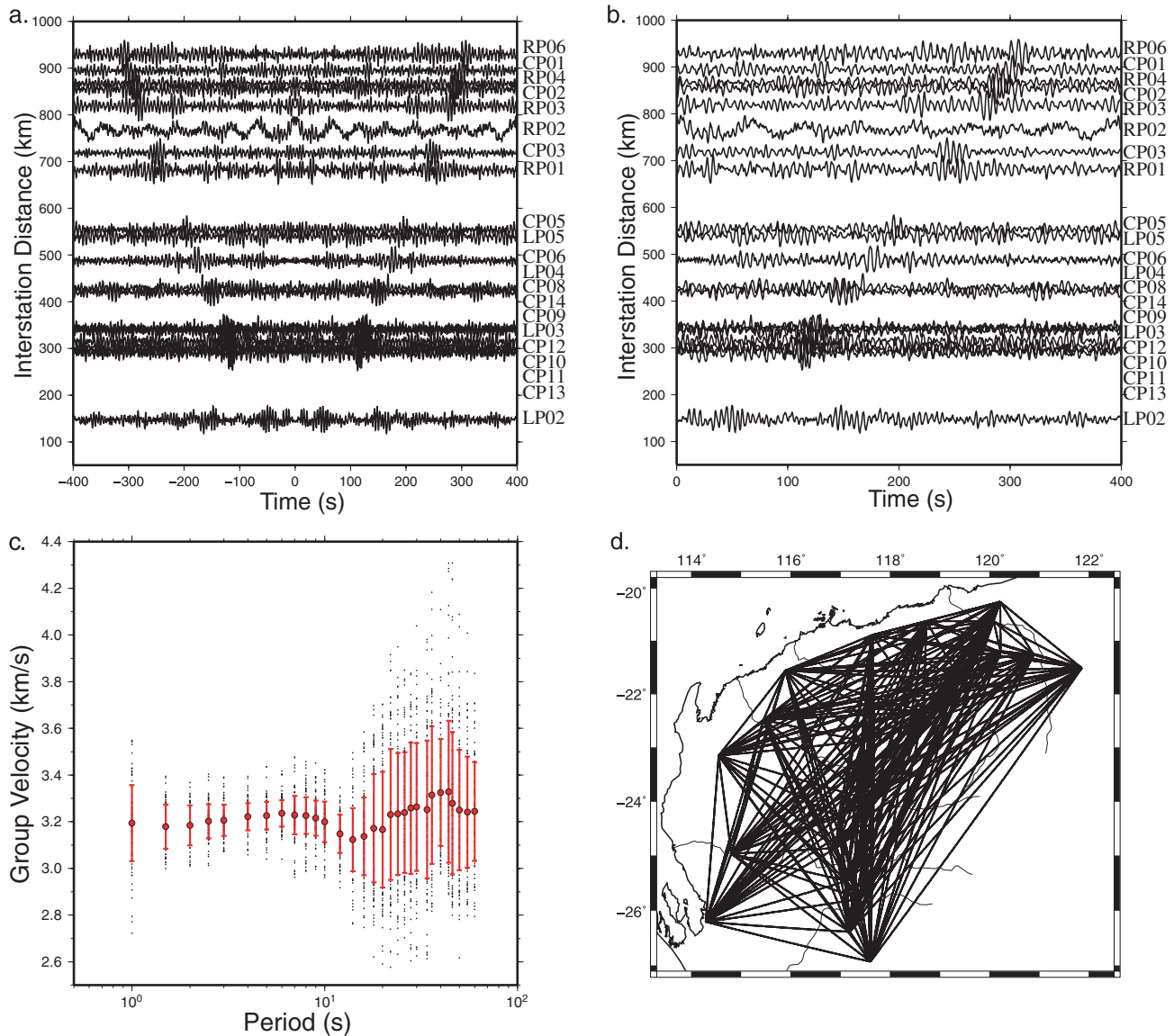


**Figure 3.** (a) All ambient noise cross-correlograms associated with station LP01. (b) The causal half of the symmetric component of the cross-correlograms associated with station LP01. (c) Average group velocity curve with error bars in red showing one standard deviation of the range of velocities at each period. (d) All possible ray paths between the CAPRA/LP array station pairs.

2001), which does not affect the dispersion measurements. Using an automated phase-matched filtering technique described in depth by Levshin & Ritzwoller (2001), group velocities are extracted for periods between 1 and 50 s (Fig. 3). We can assume that the phase shift resulting from the differentiation minimally affects the group velocity signals of a high quality cross-correlogram (Yao *et al.* 2006). Therefore, the average of the measurements from the differentiated and un-differentiated cross-correlograms is used as long as the two measurements do not vary from each other by more than 3.0 per cent. If the difference is greater than 3 per cent, the velocity measurement is rejected entirely. This promotes the utilization of only high quality data (Arroucau *et al.* 2010). In another effort to preserve only the reliable waveforms, a signal-to-noise ratio (SNR) greater than 3 and an interstation spacing of at least 3 wavelengths is made a requirement (Bensen *et al.* 2007).

Group velocity curves are calculated from the Green's function corresponding to a given model station (CP14, CP12, CP08, CP03, or LP03) and LP01, whose location approximates that of the earth-

quake. In this manner, we are able to obtain a dispersion curve that represents the average structure between source and receiver (the small red circles in the bottom right portion of Fig. 6). The range of periods providing reliable dispersion information varies from station pair to station pair according to the SNR of the filtered Green's function and the interstation distance. The Green's functions associated with the pairs CP12 and LP01, and LP03 and LP01, have poor SNRs. We thus employ a different method that aims to extract the average dispersion curve representing the Earth directly beneath the station. Cross-correlograms are calculated for all possible station combinations. The resulting set of Green's functions are then passed through a series of filters and the travel times for each receiver–receiver path at a range of periods can be measured using the phase-matched filtering technique of Levshin & Ritzwoller (2001). A fast marching surface wave tomographic inversion scheme (Rawlinson & Sambridge 2004a,b) is then applied to the measured travel times used to estimate velocity variations for different periods across the WA region (Fig. 4a). This iterative,

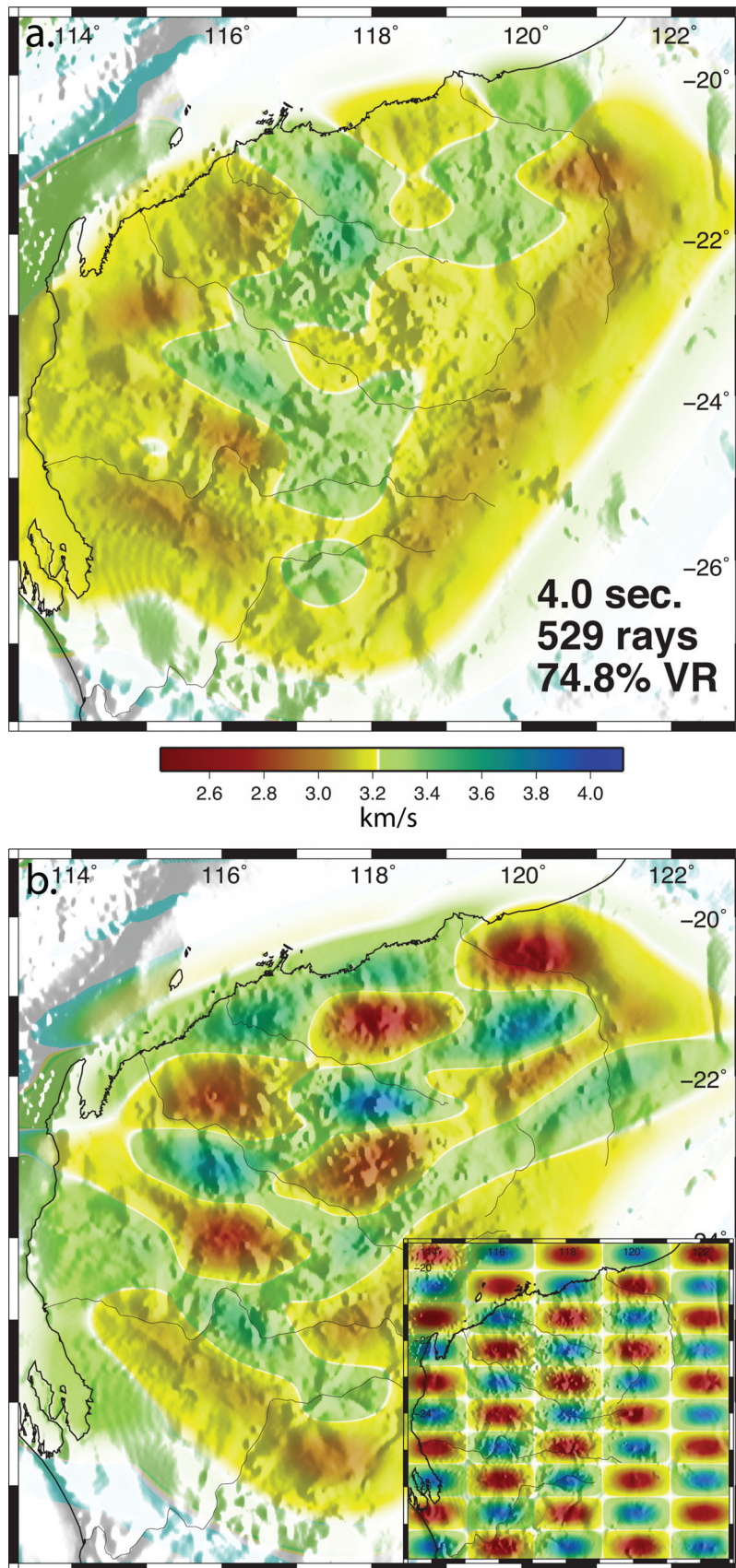


**Figure 4.** (a) 4.0 s group velocity map of Western Australia. Period, number of ray paths, and VR of the travel time residuals are shown in the lower left corner. (b) Checkerboard resolution test. The input of the checkerboard tests is an alternating pattern of positive and negative velocity squares with a maximum perturbation of  $0.8 \text{ km s}^{-1}$ .

nonlinear approach uses cubic B-splines to describe the velocity continuum and provides stable, robust solutions even in heterogeneous media. Significant improvement in traveltime residual misfit is seen for maps associated with periods between 1.5 and 14 s, with VRs ranging from 41 to 77 per cent. The lower VRs are associated with the longest- and shortest-period ( $>9$  s and  $<2$  s) solutions, where there is a gradual degradation of dispersion measurements. Synthetic ‘checkerboard’ resolution tests are performed in order to access the resolving power of the data. Gaussian noise with a standard deviation of 0.15 s is added to the synthetic data to simulate the noise content of the observed traveltimes. Fig. 4(b) displays the results of a checkerboard resolution test for a period of 4 s. The group velocity value corresponding to a given station location is extracted from each of the different period group velocity maps. These values are then interpolated to produce a group velocity curve that is representative of the lithosphere beneath the given station.

The general pattern of lower velocities in the coastal regions of WA can likely be attributed to a layer of surface sediments. The work of Abdulah (2007) provides a 3-D  $P$ -wave velocity perturbation map of northwest Australia derived from traveltimes of both local and teleseismic events. The relative velocity patterns evaluated at 35 km depth largely agree with our longer period maps ( $\sim 30$  s period), which roughly sample the same depth. The north Pinjarra Orogen and the Glenburg terrane (west of the Capricorn Orogen) (Fig. 1b) demonstrate significantly lower velocities, which correspond to the generally younger geological structures of WA.

### 3.2.2 Phase velocity from the two-station method

Phase velocity information provides a much better constraint on average shear velocity than just group velocity alone, as multiple phase velocity curves are possible for each group curve (Aki & Richards 2002). Consequently, the two-station method is employed to measure fundamental-mode Rayleigh phase dispersion curves between 10 and 60 s. In order to safely assume that the influence of

the structure between the source and nearest station is negligible, the two stations must be on approximately the same great circle path with the source (Knopoff *et al.* 1966). We require that the azimuthal difference between the earthquake to the two different stations and the azimuthal difference between the earthquake and the nearest station, and the nearest station to the farther station be less than  $2.0^\circ$ . To promote reliability in measurements at longer periods, the inter-station distance is required to be at least half of the wavelength (Yao *et al.* 2006).

We obtain 29 reliable phase velocity dispersion curves from earthquakes from Indonesia, Tonga-Fiji, and Japan with a magnitude between 5.0 and 7.0 and a depth of less than 100 km for four different station pairs: LP01 and LP03; CP08 and CP14; LP01 and CP08; and LP01 and CP03 (Fig. 5; Table 1). An average phase velocity curve is obtained for each of the four sets. The CP08 model [see the blue triangles in Fig. 6(c) for the phase dispersion curve] incorporates the curves from the path connecting LP01 and CP08; the CP03 model uses those connecting LP01 and CP03, and the LP03 model uses those connecting LP01 and LP03 stations. The models for stations CP14 and CP12 [see the blue triangles in Fig. 6(a), (b) for the phase dispersion curves] incorporate the curves from the path connecting CP14 and CP08 due to a lack of quality data associated with the LP01 to CP14 and LP01 to CP12 path. Although a phase velocity analysis using ambient seismic noise was attempted, the  $2\pi$  phase ambiguity factor prevents confident identification of the fundamental mode phase curves. Such analysis would require the use of a global 3-D model or observed, local phase velocity maps to roughly predict phase speeds (Bensen *et al.* 2007).

### 3.3 Joint inversion of teleseismic and ambient noise data

After the average phase and group velocity dispersion curves are compiled for each intended model station, a joint inversion of RF and dispersion data is performed (Fig. 6). The first step involves

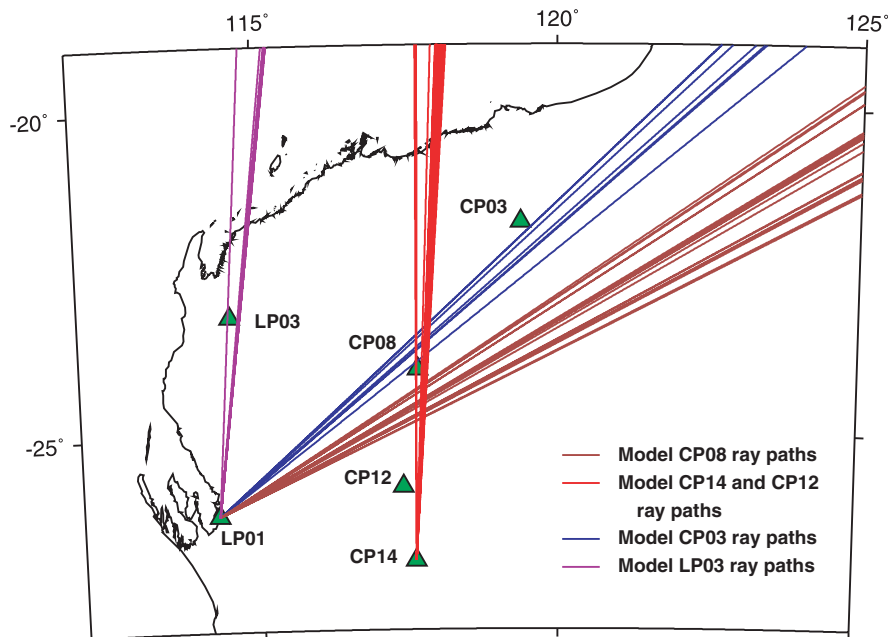


**Figure 5.** Great circle paths for station-event pairs used in the two station method of phase velocity dispersion curve retrieval are shown by coloured lines. Events are from Japan, Tonga-Fiji, and Indonesia. The ray paths associated with each model in the legend refer to the teleseismic waveforms that are analysed to determine phase velocity curves for the 1-D Earth model(s) associated with the mentioned stations.

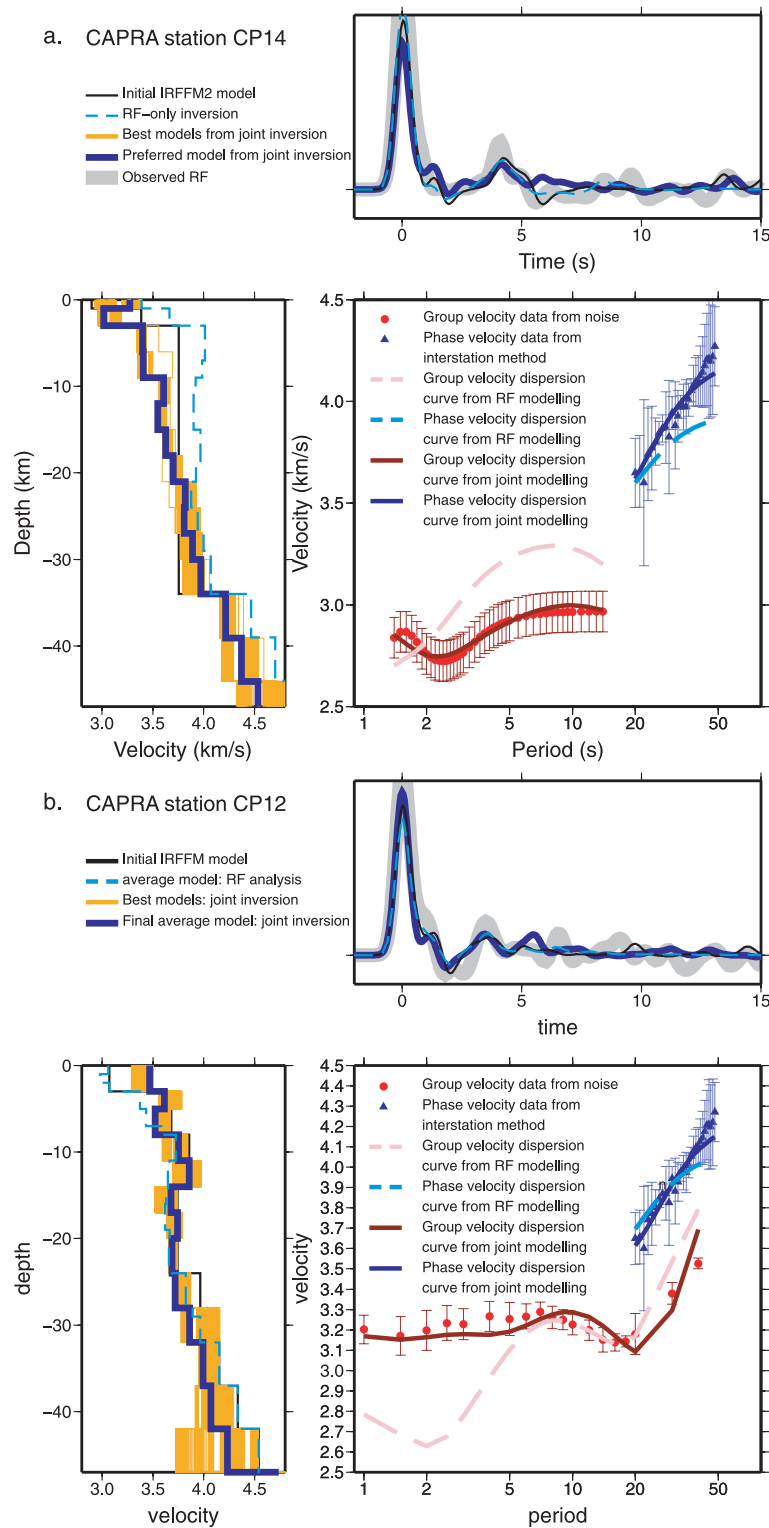


**Figure 6.** Derived 1-D shear wave velocity models for: (a) station CP14 and (b) station CP12 (c) CP08 (d) CP03 and (e) LP03 are shown in the lower left. The black line represents the initial model as produced with IRFFM2 (Tkalčić *et al.* 2011b). An ensemble of best models (yellow) comprise 279 individual models, which include three weight values (0.8, 0.9, and 0.95 for CP14; 0.5, 0.6, and 0.7 for CP12; 0.4, 0.5, and 0.6 for CP08; 0.3, 0.4, and 0.5 for CP03; and 0.2, 0.3, and 0.4 for LP03), three damping values (0.01, 0.1, and 1.0), and iterations 10 through 40. The average model obtained from RF modelling only is shown by the dashed, light blue line. The preferred (final) model obtained as an average of the best models is shown in thick dark blue line. In the upper right, the observed RF is shown by the thick gray line. The initial IRFFM2 model produces the RF denoted by the black line. The average RF obtained from the RF inversion is shown by the dashed light blue line. The final RF resulting from the joint inversion of RF and dispersion information is shown by the solid dark blue line. In the bottom right, the blue triangles denote phase velocity data obtained from the two-station method. Red circles represent group velocity information obtained from ambient noise analysis. Error bars show one standard deviation of the velocities. The curves resulting from just the RF modelling are shown by the dashed pink and light blue lines. The final group and phase velocity dispersion curves are shown by the solid red and blue lines respectively.

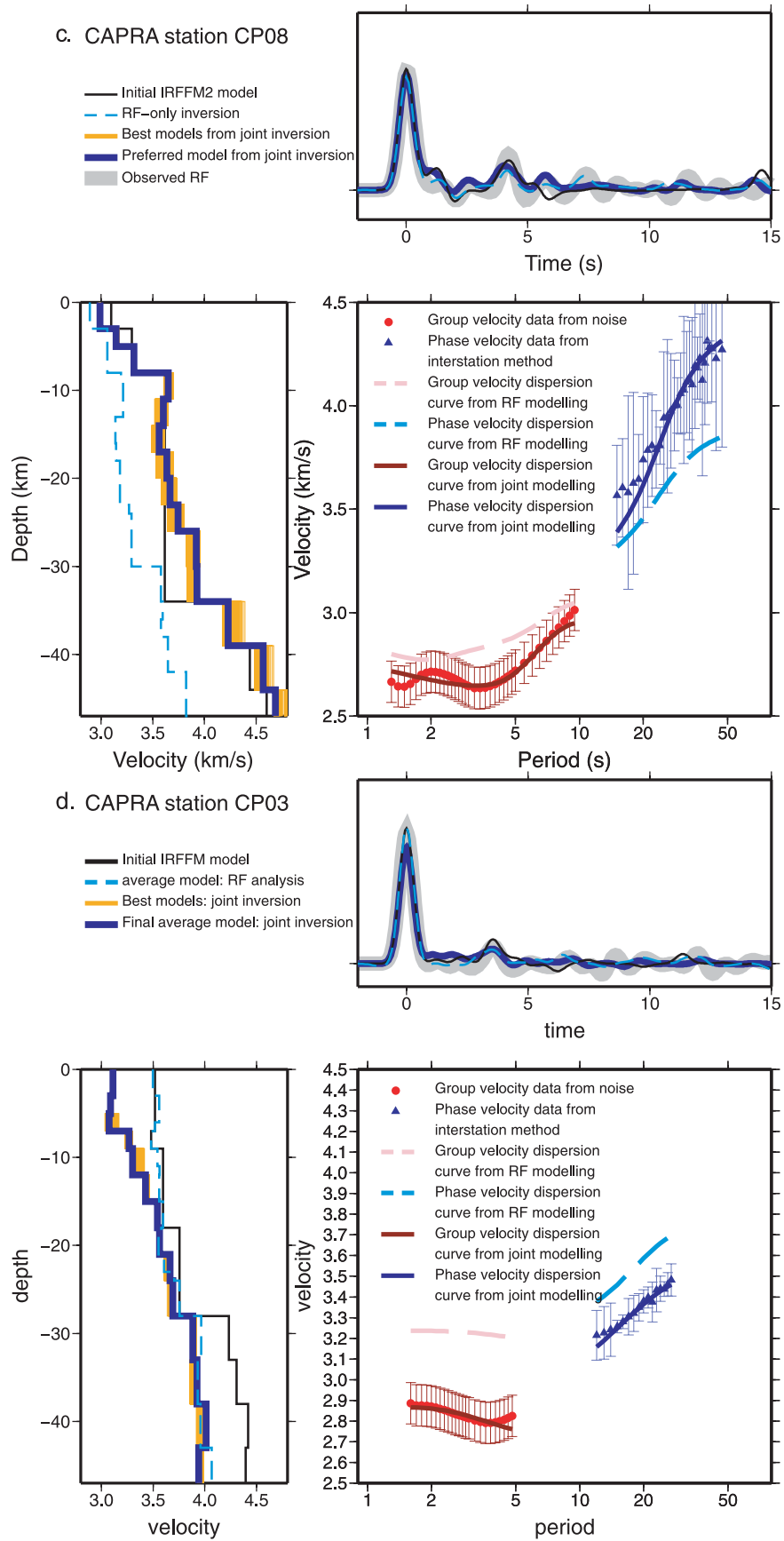


Figure 6. (Continued).

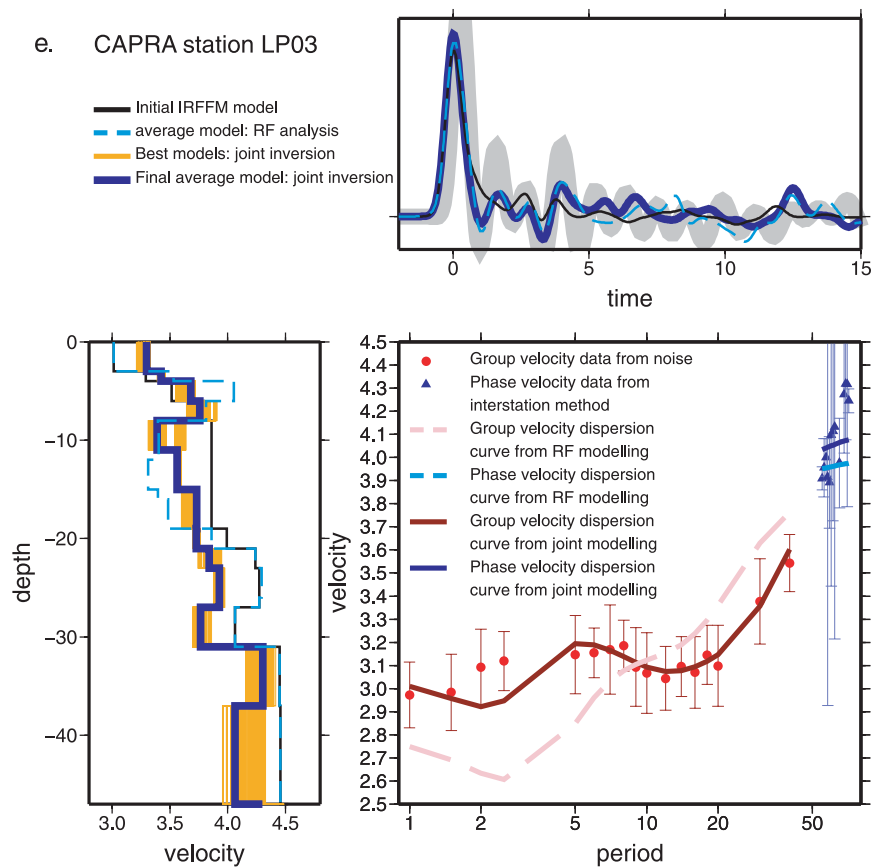


Figure 6. (Continued).

using the interactive forward modelling software for joint modelling of RFs and surface wave dispersion curves IRFFM2 (Tkalčić *et al.* 2011b) to create a simple and reasonable initial model. In this process, the average model from the RF inversion is altered manually until the synthetic RF better fits the dispersion data while still maintaining good agreement with the RF data. Then we linearly invert the fundamental-mode group and phase velocities simultaneously with the radial RFs for a shear wave velocity profile beneath each station (Fig. 6) (Herrmann 2004) using our initial model resulting from the forward modelling. Our approach is similar to that of Julia *et al.* (2000, 2003). A fixed bottom layer below 47 km, which approximates the lower limit of the RF and dispersion curve sampling depth, is used to focus the inversion sensitivity on the uppermost lithosphere. A time window of  $-5.0$  to  $15.0$  s is used to invert the RFs to concentrate the inversion on the Moho character. The dispersion curves are sampled at period intervals between  $0.1$  (at shorter periods) and  $1.0$  s (for longer periods), and the RFs are sampled every  $0.05$  s. Differential smoothing is applied while an influence parameter controls the relative weight between the dispersion curves and RF data. We then run a series of inversions, each with an influence parameter ranging between  $0.0$  and  $1.0$  (where  $0.0$  indicates only an inversion of RF data, and  $1.0$  only inverts dispersion data). We choose the models resulting from the weight value that best balances the individual fits of the dispersion and RF data, meaning that the percent of data misfit is approximately equal for both these datasets. Successive inversions converge after about five iterations; however, the final model is created by the average of it-

erations 20 through 40, in which range no discernible improvement in VR is seen.

Our final jointly inverted models agree well with previous studies and, moreover, provide further constraints on the upper lithosphere of WA. The general pattern of increased Moho depth beneath the Capricorn Orogen and thinner crust under the cratons is consistent with the work of Reading *et al.* (2011). Upon jointly inverting for the Capricorn Orogen structure associated with station CP08, the Moho depth estimate increases from  $30$  km (resulting from the RF analysis) to  $34$  km (the dashed light blue line and solid blue line of Fig. 6c), which agrees more closely with Reading *et al.* (2011), who estimated the Moho to be at  $36$  km depth. This change arises due to a trade-off between the absolute velocity and the thickness of the crust when only information from RFs is available. Due to the fact that long period phase velocity dispersion data brings additional information about the absolute velocity of the lower crust [faster in this case; Fig. 6(c)], the crustal thickness increases to accommodate the faster propagation of shear waves through the crust.

While no previous studies have performed a high-resolution group or phase velocity analysis of WA, Saygin & Kennett (2010) completed a set of continental-scale group velocity maps using ambient noise for periods between  $5$  and  $12.5$  s. Our results are in rough agreement in that upper crust group velocities range from  $2.8$  to  $3.4$  km s $^{-1}$ . We improve the constraints by increasing resolution and including phase velocity information derived from the two-station method. For the first time, RFs are analysed for the Pinjarra Orogen. Although the data are very noisy for these coastal stations,

we are able to obtain a rough estimate of crustal structure and Moho character for the area.

#### 4 MOMENT TENSOR INVERSION OF THE SHARK BAY EVENT

Equipped with a collection of upper lithosphere models of WA, we are now ready to perform a full waveform inversion for source properties of regional earthquake recordings. After first using the Earth

reference model *ak135* (Kennett *et al.* 1995), we will then use our own models to produce synthetic Green's functions and compare them with the filtered observed waveforms. It is assumed that the Green's functions resulting from our composite model represent the average structure between the source and each station. To represent Earth structure associated with stations CP14 and CP13, we use the model CP14; for stations CP12, CP11, CP10, and CP09 we use the model CP12; for stations CP03, CP05, CP06 we use the CP03 model; and stations LP03 and CP08 each have their own model.

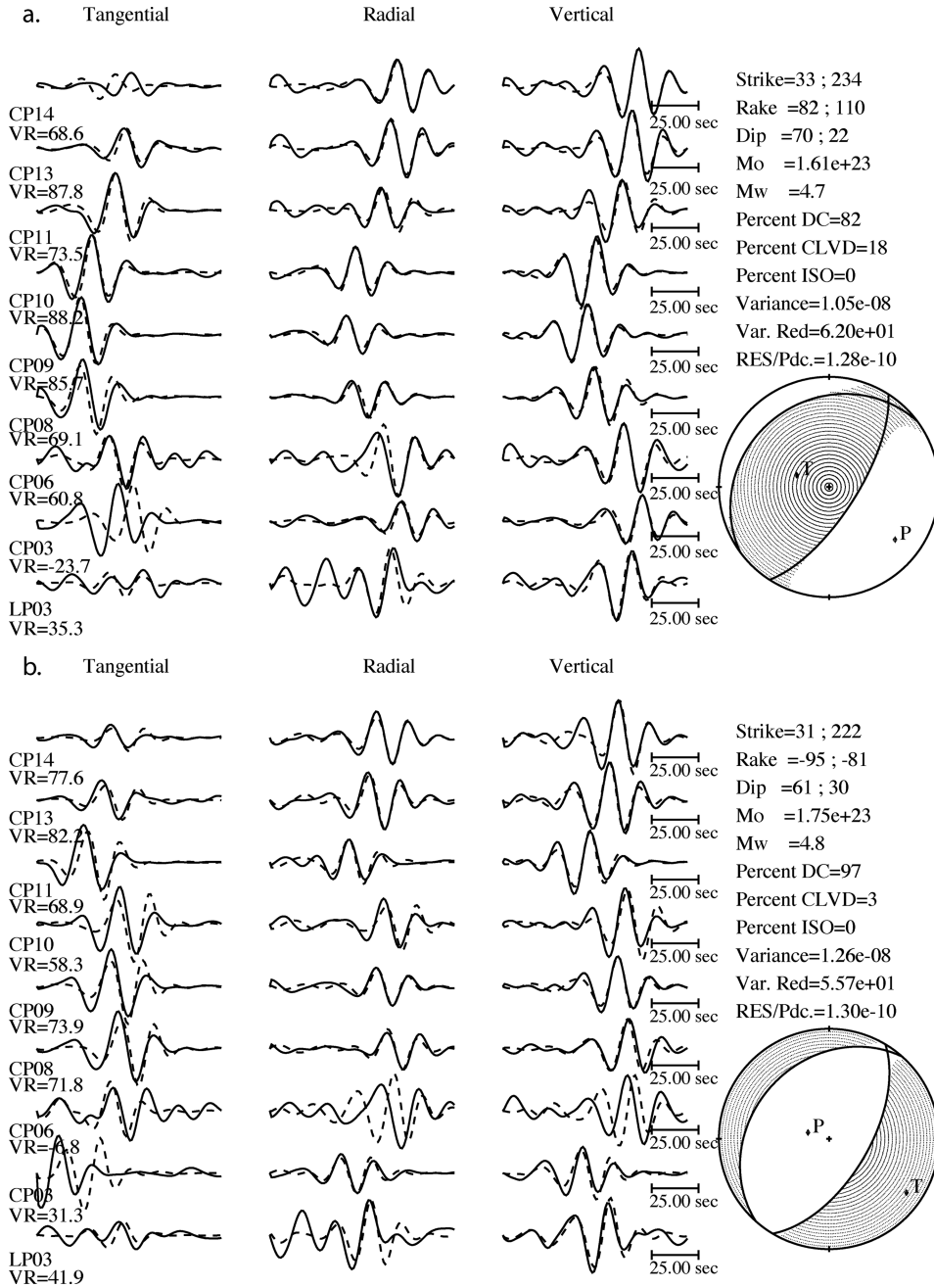


**Figure 7.** Results of moment tensor inversion for the case in which a single 1-D model [(a) model *ak135* and (b) model CP14] is used to produce structural Green's functions for nine selected stations. The solid lines show the observed waveforms filtered between 15 and 35 s, whereas the dashed lines are the synthetic waveforms filtered in the same manner. The three different components of the seismograms are shown from left to right: tangential, radial, and vertical. The lower-hemisphere projection of the *P*-wave radiation pattern is shown in the lower right along with the pressure (*P*) and tension (*T*) axis. The strike, rake, and dip of the two nodal planes along with the scalar seismic moment, moment magnitude, percent double couple (*DC*), *CLVD*, and isotropic (*ISO*) of the best solution are listed on the right.

#### 4.1 Method

Using upper lithosphere models for CP14, CP12, CP08, CP03, and LP03 (Table 1), we employ a frequency-wavenumber integration program developed to calculate synthetic Green's functions (Saikia 1994) from plane-layered models. Respective moment tensors are estimated using full waveform regional moment tensor inversion (Dreger & Helmberger 1993), which uses long-period three-component waveforms at regional distances. This method of waveform inversion solves for the moment tensor elements through a linear inversion in the time-domain that seeks to minimize the difference between synthetic and observed waveforms. Small time-shifts specific to each station are used to best align the data with the synthetics and to minimize the effect of earthquake mislocation errors and uncertainties in the average velocity structure. The earthquake depth is solved for iteratively. Instrument response is removed from the data, and both synthetics and data are bandpass-filtered be-

tween 15 and 35 s, which best isolates the body and surface waves. The extensive study of Earth structure justifies the attempt to fit higher frequency signals. A source depth of 18 km ([www.ga.gov.au](http://www.ga.gov.au)) is used in the initial inversion. The inversion procedure we adopt here considers only the deviatoric tensor, neglecting volumetric changes of the source. The earthquake is assumed to be a point source in time and location, which is a reasonable approximation for far-field waveform modelling of the Shark Bay event ( $M_L = 5.3$ ). Solutions are judged based on both VR and percent double-couple. The accuracy of the depth estimate given by GA is tested through a series of iterations, each imposing a different depth.

#### 4.2 Results

After an extensive analysis and consideration of all stations, only the nine least noisy stations (LP03, CP14, CP13, CP11, CP10, CP09,

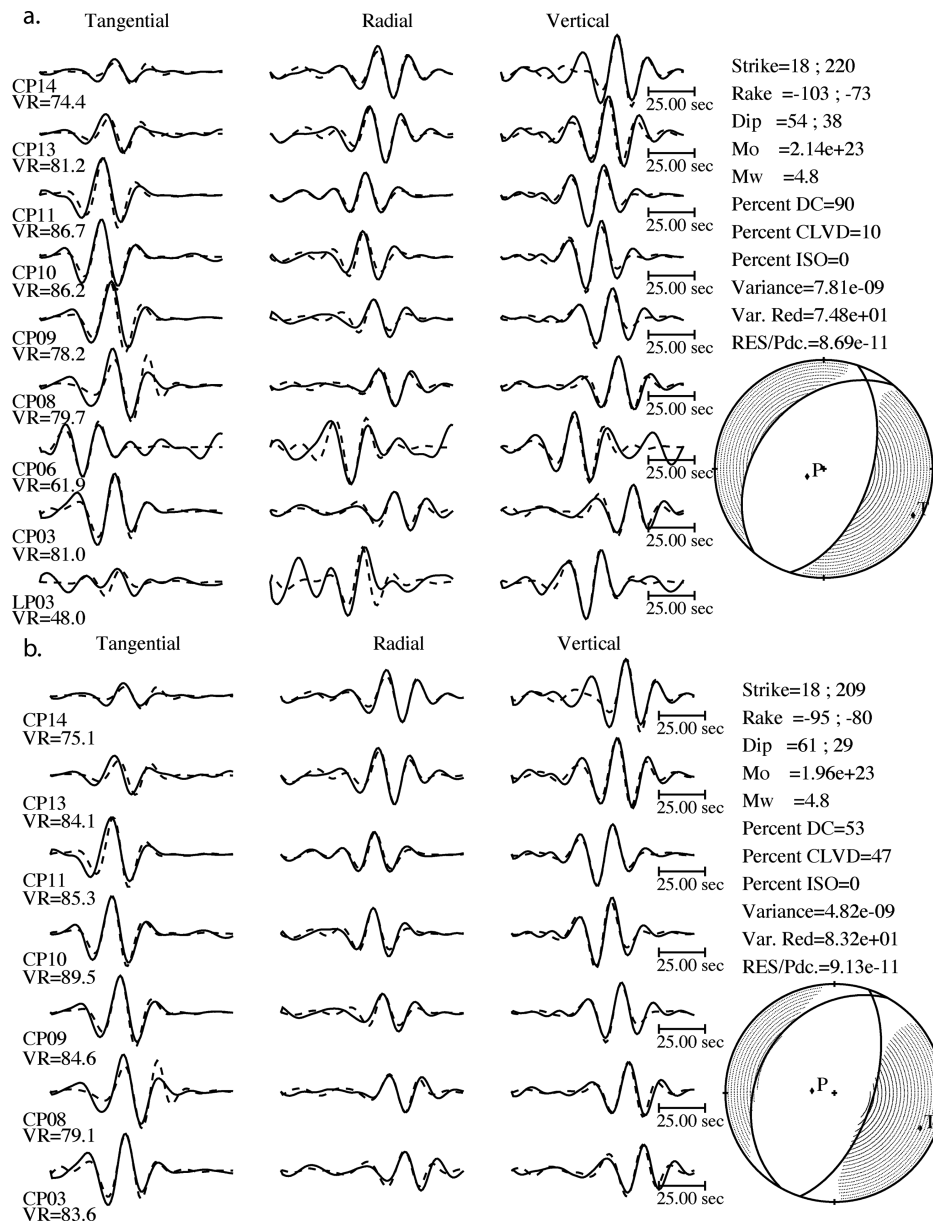


**Figure 8.** Results of moment tensor inversion for the case in which a composite 1-D model is used to produce structural Green's functions for the total of: (a) nine and (b) seven stations. For the explanation of waveforms, focal mechanism plot and the legend, see captions of Fig. 7.

CP08, CP06, and CP03) are used in the inversion. The inclusion of the more noisy stations does not significantly improve the azimuthal coverage and, moreover, does not help to constrain the solution. For example, stations CP12, CP05, and LP01 were disregarded in the inversion due to low SNRs at the time of the earthquake in this study. Other disregarded stations were distant from the source, and the waveforms were too noisy for analysis.

In this section we describe the results of waveform inversions using different structural models. We first invert the waveforms of the nine remaining stations using only the Earth reference model *ak135* (Kennett *et al.* 1995). The best-fitting moment tensor has fault planes with strikes of  $33^\circ$  and  $234^\circ$ , dips of  $70^\circ$  and  $22^\circ$ , rakes of  $82^\circ$  and  $110^\circ$ , and a VR of 62.0 per cent (Fig. 7a). We then perform the inversion using only the model CP14, which is a robust model and a good approximation for much of the region (Fig. 6a). The best-fitting moment tensor has fault planes with strikes of  $31^\circ$  and  $222^\circ$ , dips of  $61^\circ$  and  $30^\circ$ , and rakes of  $-95^\circ$  and  $-81^\circ$ ; the VR is only 57.8 per cent (Fig. 7b). Previous experience in

inverting waveforms for the seismic moment tensor in a complex tectonic setting suggests that it is possible to improve the overall fit by using a composite model (Tkalčić *et al.* 2009). A composite model approach is also used in a routine moment tensor inversion in California, where the Earth structure connecting the earthquakes occurring in the Mendocino triple-junction with the stations is quite different from that used to produce Green's functions associated with the Sierra Nevada events (Pasyanos *et al.* 1996). Therefore, we test whether a composite model improves the goodness of fit in our situation. When using a composite model constructed from the five individual models described in section 3.3, the VR increases to 74.8 per cent, and the solution is 90 per cent double couple (Fig. 8a). The best-fitting moment tensor remains similar to that obtained using the single CP14 model (planes with strikes of  $18^\circ$  and  $220^\circ$ , dips of  $54^\circ$  and  $38^\circ$ , and rakes of  $-103^\circ$  and  $-73^\circ$ ). The moment magnitude is modelled at  $M_w$  4.8; which is in agreement with the work of Allen *et al.* (2011) on  $M_w$  and  $M_L$  magnitudes for central and western Australian earthquakes. He found that the  $M_w$

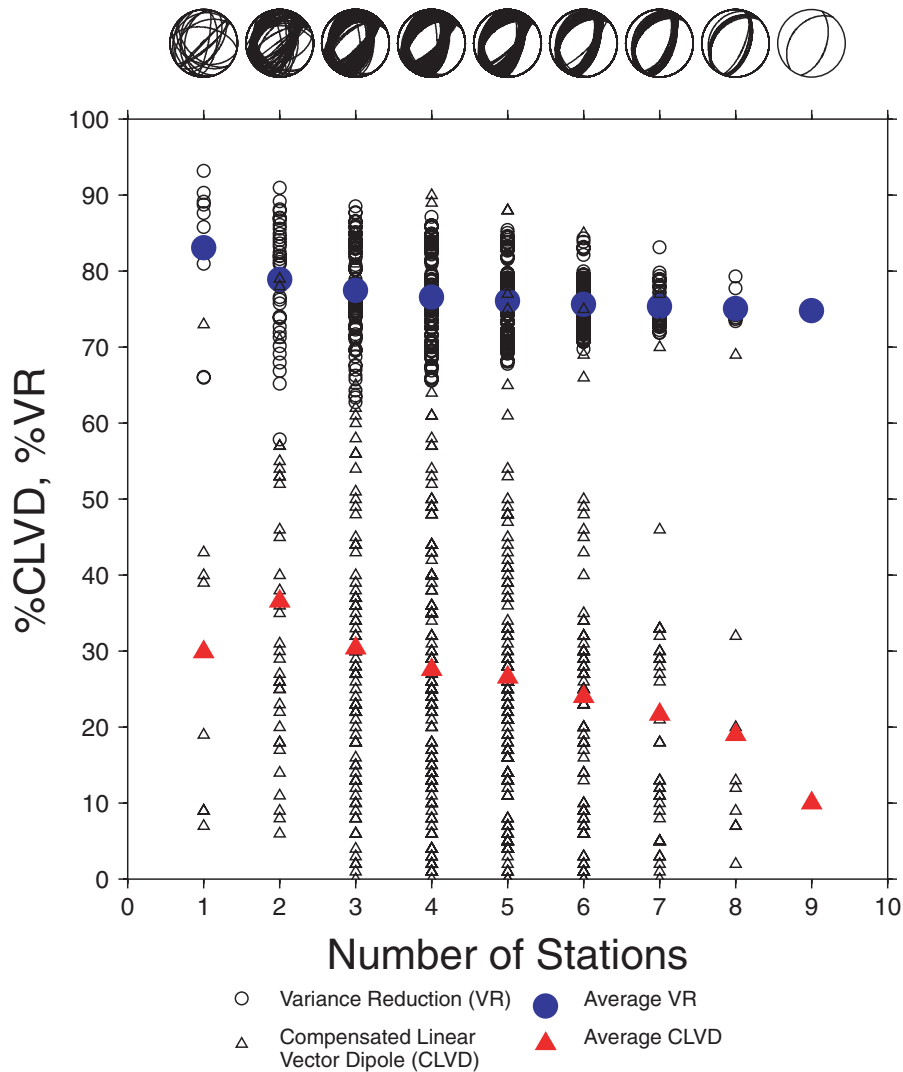


**Figure 9.** Jackknife sensitivity test for nine selected stations mentioned in the text. The blue circles indicate the average VR between synthetic and observed waveforms as the number of stations increases from one to nine. The red triangles represent the average CLVD, defined as 100 per cent less the percentage of double couple. The empty circles show individual VRs for different combinations of each number of stations, and the empty triangles show the corresponding per cent CLVDs. The resulting focal mechanism solutions for each number of stations are superimposed upon each other and displayed at the top of the figure.

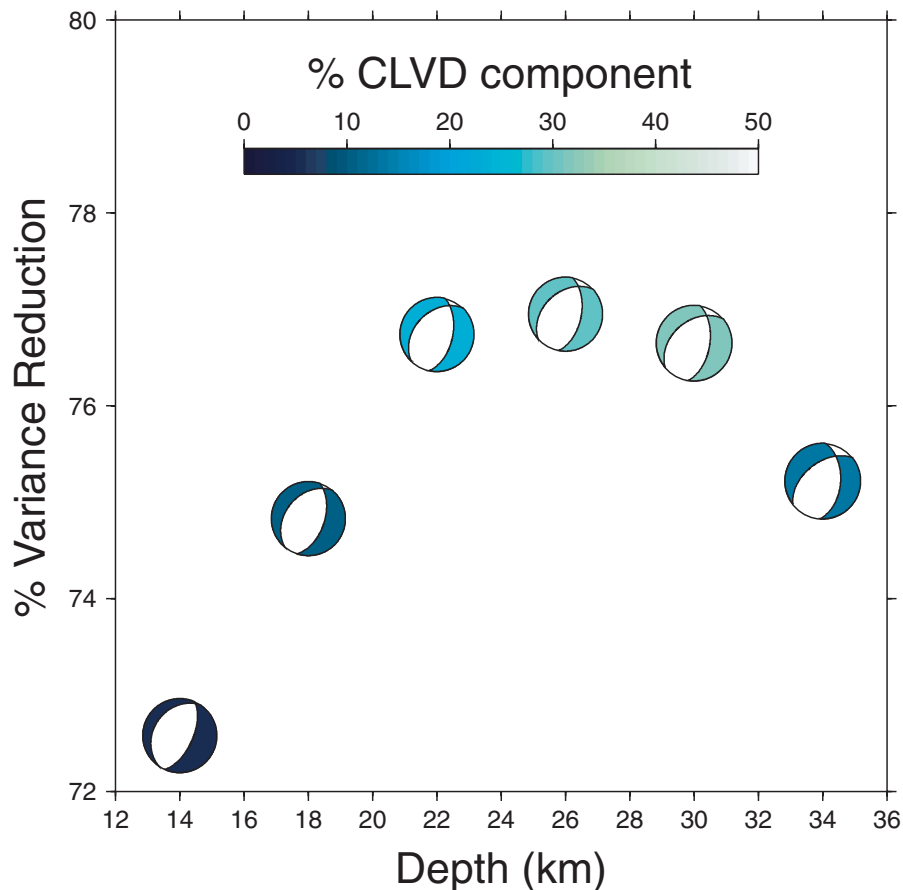


**Figure 10.** A depth-sensitivity test for a combination of the nine selected stations mentioned in the text. The focal mechanisms for the best solution assuming the source originated at various depths of 14, 18, 22, 26, 30, and 34 km are shown. The quadrants associated with the tension-axes are coloured according to the percent of CLVD, defined as 100 per cent less the percentage of double couple. The initial estimate as quoted by GA is 18 km.

of a WA events is typically 0.3 to 0.5 magnitude units smaller than the corresponding  $M_L$  estimate.

Fig. 9 shows the results of a jackknife sensitivity test with the selected nine stations. This test is designed to reveal if any one station, or small subset of stations, is dominating the solution mechanism. This does not appear to be the case, and the solution becomes increasingly invariant as the station combination changes once three stations are included in the inversion. The average VR decreases by only 9 per cent as station number increases from one to nine, indicating the robustness of the solution. The percent compensated linear vector dipole (CLVD), which represents the percentage of the solution that is non-double-couple in a deviatoric moment tensor, decreases with increasing number of stations as the solution becomes increasingly well constrained. However, at least eight stations are required to considerably reduce the scatter in CLVD per cent and reduce the estimate below 20 per cent.

LP03 has the poorest signal to noise ratio of the chosen nine stations, but we experiment with including this station in the inversion as it significantly improves azimuthal coverage. If we remove LP03 from the inversion, the moment tensor changes only very slightly, and the VR increases to 79.3 per cent; however, the percent double couple drops to 68 per cent, which could be a result of spurious effects caused by insufficient azimuthal coverage (e.g. Šilený *et al.* 1996). We can improve the VR further by excluding another noisy station, CP06, from the inversion. This combination of seven stations yields a VR of 83.2 per cent, but contains only 53 per cent

double couple (Fig. 8b). For all three scenarios, the  $M_w$  estimate is 4.8, and the moment tensor is an oblique normal fault.

The results of the depth analysis are shown in Fig. 10. Although it is not likely that the actual depth is lower than 18 km, the upper limit on the acceptable range is more ambiguous. The best VR is achieved for depths between 22 and 30 km; however, the percent double couple decreases significantly as depth increases between 18 and 30 km, which is less likely if we assume the earthquake has a simple tectonic character.

## 5 DISCUSSION

A series of sensitivity tests were performed to assess the reliability of the inversion method. Synthetic waveforms are generated utilizing the E3D finite difference method (Larsen & Schultz 1992) using our preferred orientation of nodal planes (Fig. 8a) (strike  $18^\circ$ , dip  $54^\circ$ , and rake  $-103^\circ$ ), a  $M_w$  of 5.0, and our CP14 structure model. The synthetics are processed in the same manner as the observed data. Using the same crustal model and hypocentre location, Green's functions are created and compared to the synthetics. As expected, we recover the same moment tensor with 100 per cent VR when using the nine station locations used in the actual inversion of the Shark Bay event.

To assess the effect of noise on the solution, white noise with a root mean square of 150 per cent of the peak amplitude of the signal is added to the synthetic data. Again the inversion is performed on

the synthetic data. The strike, dip, and rake vary by at most 4° from the input mechanism. The estimated magnitude is 4.9, the percent double-couple is 95 per cent, and the VR decreases to 54.1 per cent. The general character of the solution does not seem to be strongly affected by noise in the data; nonetheless, it is a likely cause of a low VR.

After describing the process behind obtaining our full waveform solution, we now provide comparisons with first motion data. Revets *et al.* (2009) presented a first motion estimate (nodal plane 1: strike 60.0°, dip 60.2°; nodal plane 2: strike 258.9°, dip 31.2°), which corresponds to a reverse thrust fault scenario, and has a station distribution ratio (STDR) (Reasenber & Oppenheimer 1985) of 0.6. This quality measurement depends on the distribution of the stations relative to the radiation pattern. A low STDR is caused by polarity observations from stations near nodal planes and lack of complete azimuthal coverage. According to Kilb & Hardebeck (2006), a STDR > 0.65 is preferred when identifying quality mechanisms. In addition, a closer look into the waveforms recorded at CAPRA/LP and other available broad-band stations (Tables 1 and 2) reveals an emergent character of first motions, making most polarity readings very ambiguous (Fig. 12). We used take-off angles based on *ak135* (Kennett *et al.* 1995) in our first motion analysis, while simple region-specific crustal models were used in the analysis of Revets *et al.* (2009). The disagreement in solutions can be in part attributed to this difference. Another contributing factor is the selection of stations used in the two analyses. We included stations from Antarctica and Kyrgyzstan, which provide unique azimuthal coverage and, therefore, have a large effect on the first motion solution. The Revets *et al.* (2009) analysis incorporated data only from Australia-based stations. As a means of further discriminating between the reverse and normal solutions, we compare the synthetic waveforms computed with the focal mechanism of both our preferred solution (normal fault) and that of Revets *et al.* (2009) (reverse fault) (Fig. 11). The average cross-correlation coefficient (when assuming the absence of anisotropy) is 0.57 for the reverse solution and is 0.87 for the normal solution. Of equal importance, however, is that for several stations (CP06, CP08, and CP09), the cross-correlation coefficients associated with the reverse solution are negative for the tangential component of the waveforms, likely indicating an inability of the focal mechanism solution of Revets *et al.* (2009) to reproduce the observed waveforms.

A bootstrap analysis of the first motion based on previous experience and recommendations presented in Diehl & Kissling (2007) and using the FOCMEC software package of Snoko (2003) shows a high level of uncertainty in determining the orientation of nodal planes. Following Diehl and Kissling (2007), a high-pass filter (corner frequency 1.0 Hz) is applied to all broad-band channels to remove long period noise. Fig. 12 shows a sampling of the waveforms used in the first motion analysis superimposed on our preferred solution from the full waveform moment tensor inversion. Table 1 and 2 list all stations used. For the majority of selected recordings it is very difficult to identify a first arrival and, moreover, determine its polarity. Our conclusion is that the first motion solution is not robust and cannot diminish the waveform solution on the basis that they do not agree entirely. We believe that this is an indication that the Shark Bay event is more complex than previously understood from the first motion solution. We therefore find it preferable to base a focal mechanism solution on the seismic moment tensor obtained from the full waveform inversion as we have been able to do in this detailed analysis.

There have been many studies on the stress field of WA (e.g. Coblenz *et al.* 1998; Reynolds *et al.* 2002; Clark & Leonard 2003;

**Table 2.** All stations (and respective geographical coordinates) used in the first motion analysis that are not part of CAPRA or LP arrays.

Station Name	Latitude (°)	Longitude (°)
KAKA	-12.71	132.44
KMBL	-31.37	121.88
MUN	-31.98	116.21
STKA	-31.88	141.60
WB0	-19.77	134.39
WB1	-19.96	134.35
WB2	-19.94	134.35
WB3	-19.92	134.36
WB4	-19.90	134.36
WB5	-19.88	134.37
WB6	-19.85	134.37
WB7	-19.84	134.38
WB8	-19.81	134.38
WB9	-19.79	134.38
WC1	-19.92	134.34
WC2	-19.93	134.37
WC3	-19.96	134.37
WC4	-19.96	134.34
WR0	-19.96	134.54
WR1	-19.94	134.34
WR2	-19.95	134.36
WR3	-19.95	134.39
WR4	-19.95	134.41
WR5	-19.95	134.43
WR6	-19.95	134.45
WR7	-19.96	134.48
WR8	-19.96	134.50
WR9	-19.96	134.51
MBWA	-21.16	119.73
NWAO	-32.93	117.24
AL09	-74.30	66.79
S2B5	-33.39	143.48
S2B8	-33.49	145.07
stc1	-42.15	146.47
BBOO	-32.81	136.06
CMSA	-31.54	145.69
FITZ	-18.10	125.64
FORT	-30.78	128.06
AAK	42.63	74.49
EKS2	42.66	73.78

Reynolds *et al.* 2003; Zhao & Muller 2003) that utilized data from many different sources, that is earthquake focal mechanisms, borehole breakouts, overcoring measurements, hydraulic fracture measurements, geological indicators, and drilling-induced tensile fractures. Although there is general agreement that the pressure axis in the Western Australia region runs approximately east-west, according to Zhao & Müller (2003) the Shark Bay region is within a zone of least compression (with compressive principle stress values  $\leq 0$  MPa). Therefore, it is not necessary to assume that the stress field is compressive, perhaps explaining the normal fault solution obtained for the Shark Bay event. Moreover, the work of Kagan (1992) has shown that earthquakes in tectonic blocks often weakly depend on the current deformation and tectonic stresses, and are instead more heavily dependent on known and hidden defects in the rock medium. Differently oriented pre-existing faults in the area could also provide controls on the nature of the resulting seismicity.

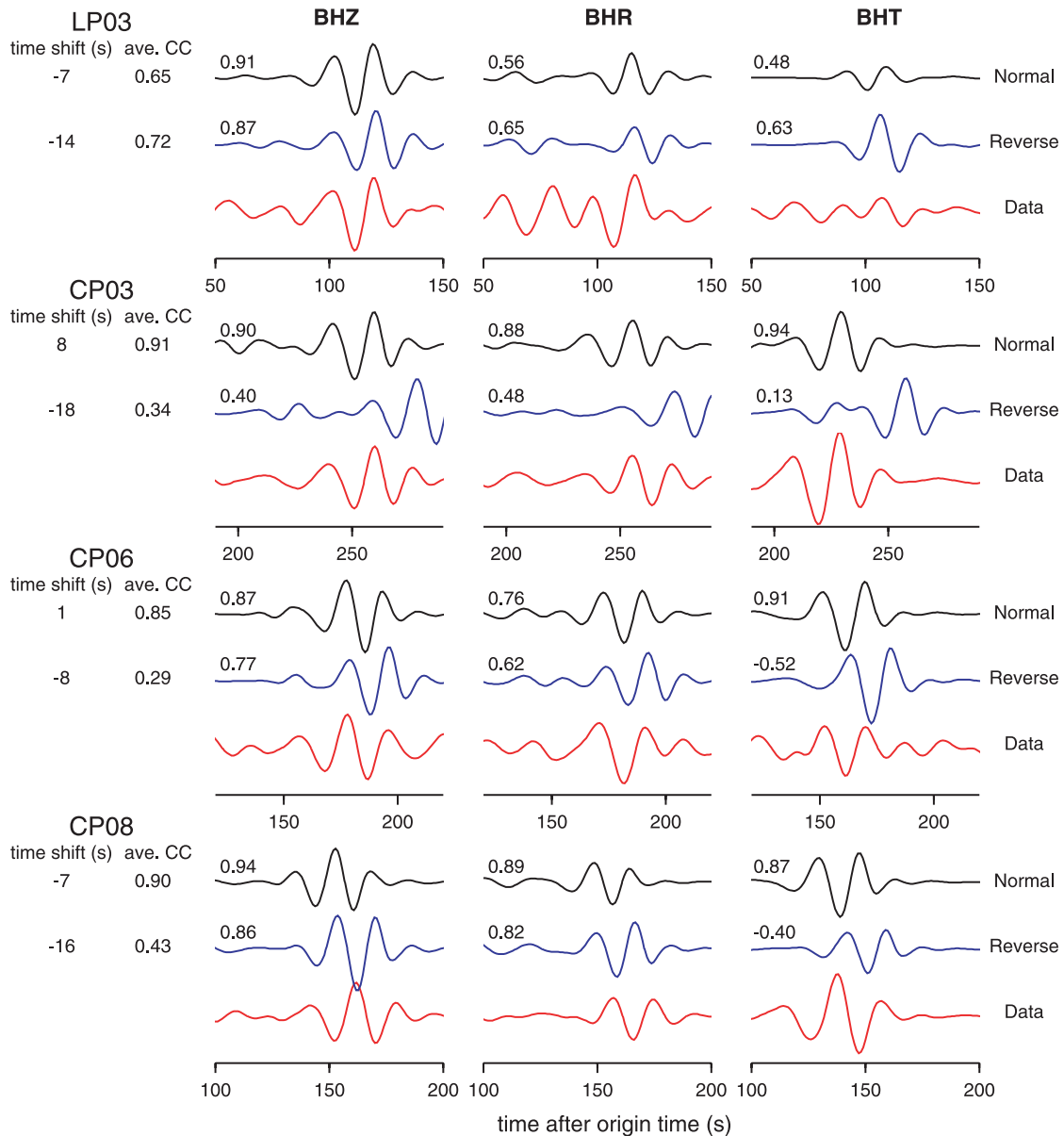


**Figure 11.** A comparison of the observed waveforms (red) to the synthetic waveforms produced from the preferred, normal focal mechanism solution (black) and from the reverse solution given by Revets *et al.* (2009) (blue). The vertical, radial, and tangential station components are shown from left to right as BHZ, BHR, and BHT. The synthetic waveforms have been shifted in time according to the number of seconds listed under ‘time shift (s)’ on the far left of the waveforms. This time-shift corresponds to the highest average cross-correlation coefficient (specified under ‘ave. CC’) between the data and synthetics for the time interval shown. The individual cross correlation coefficient between the data and synthetics corresponding to each component is listed above the individual waveforms.

## 6 CONCLUSIONS

Models of the upper lithosphere for five regional source-receiver pairs were produced from a joint inversion of RF data and dispersion data derived from distant earthquakes and ambient noise. Our 1-D models agree well with previous RF results, and improve upon existing constraints. The general character of the Moho is consistent with previous RF work, as we see a sharp, intermediate-depth Moho beneath the Pilbara and Yilgarn cratons and a deeper, less-sharp transition beneath the Capricorn Orogen. We further improve knowledge of the upper lithosphere of Western Australia by combining dispersion with RF data and by providing a shear velocity model for coastal stations. We show that a composite model enables

a more robust inversion of three-component full waveforms for the seismic moment tensor than a simple 1-D model. In particular, we calculate the moment tensor and depth of the 2007 Shark Bay, Western Australia, earthquake, and obtain a robust oblique normal solution of strike  $18^\circ$ , dip  $54^\circ$ , and rake  $-103^\circ$ . This is in agreement with the stress field of the Shark Bay area, which is in a zone of least compression. Our full waveform solution, which incorporates a composite crustal structure model of Western Australia, improves on the determination of the focal mechanism of the Shark Bay event from first motion analysis alone.

This study demonstrates how a composite 1-D model of the upper lithosphere may be developed in a low seismicity region with a limited number of seismic stations and its subsequent use can

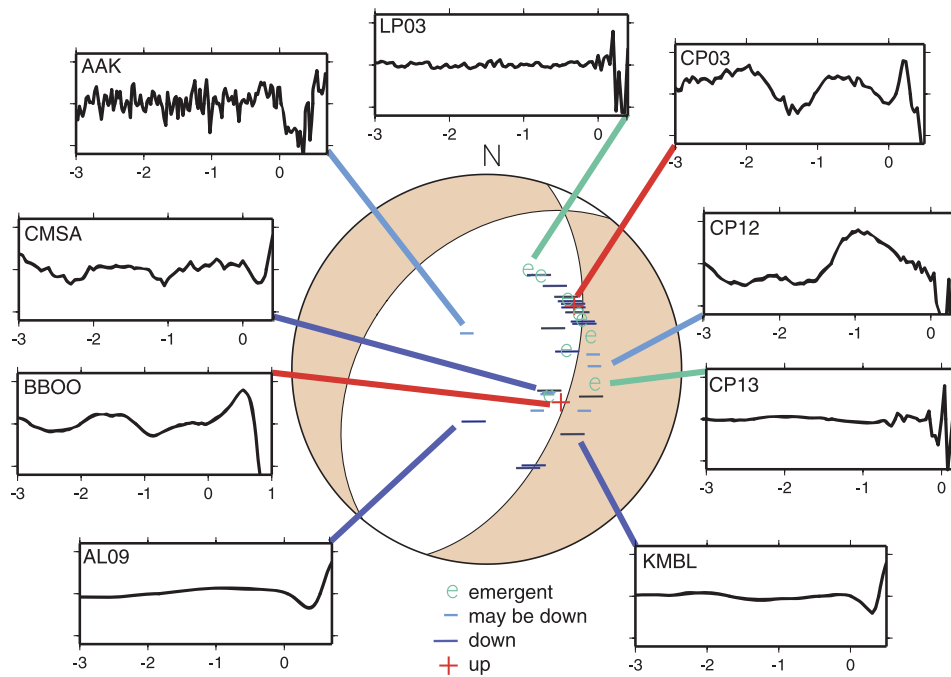


**Figure 12.** First motion polarity readings superimposed on the preferred full waveform inversion solution. The tan-coloured quadrants contain the tension axes. A sample of nine waveforms recorded at different azimuths and epicentral distance are shown to demonstrate the character of the first arrivals. Each waveform is cut to 3 s before and 1 s after our pick of the first P arrival. The waveforms are filtered with a high pass corner of 1 Hz.

improve the analysis of an earthquake's source mechanism. The methodology is widely applicable to the study of earthquake focal mechanisms in intraplate settings, where a careful determination of the focal mechanism for such rare events represents a significant advance in understanding the neotectonics of a given region.

## ACKNOWLEDGMENTS

We owe many thanks to Myra Keep and coworkers at the University of Western Australia for use of the LP data. We are grateful to Steven Sirotnjuk, Armando Arcidiaco, Cvetan Sinadinovski and Fabrice Fontaine for providing assistance in the field. Also, thanks to many land owners and station managers for allowing installation and access to station sites. We thank Pierre Arroucau for his invaluable assistance with the ambient noise analysis, Edward Leask for his insights on the RF analysis, and Brian Kennett for insightful discussions. We are also grateful for the comments provided by Jan Šilený, Sean Ford, and an anonymous reviewer.

## REFERENCES

Abdulah, A., 2007. Seismic body wave attenuation tomography beneath Australasian region, *PhD thesis*, The Australian National University, Canberra.

Aki, K. & Richards, P.G., 2002. *Quantitative Seismology: Theory and Methods*, 2nd edn, University Science Books, Sausalito, CA.

Allen, T., Burbidge, D., Clark, D., McPherson, A., Collins, C. & Leonard, M., 2011. Development of the next generation Australian National Earthquake Hazard Map, *Proceedings of the Ninth Pacific Conference on Earthquake Engineering*, Auckland, 2011 April 14–16, paper 207.

Arroucau, P., Rawlinson, N. & Sambridge, M., 2010. New insight into Cainozoic sedimentary basins and Palaeozoic suture zones in southeast Australia from ambient noise surface wave tomography, *Geophys. Res. Lett.*, **37**, L07303, doi:10.1029/2009GL041974.

Bensen, G.D., Ritzwoller, M.H., Barmin, M.P., Levshin, A.L., Lin, F., Moschetti, M.P., Shapiro, N.M. & Yang, Y., 2007. Processing seismic ambient noise data to obtain reliable broad-band surface wave dispersion measurements, *Geophys. J. Int.*, **169**, 1239–1260.

Betts, P.G., Giles, D., Lister, G.S. & Frick, L.R., 2002. Evolution of the Australian lithosphere. *Aust. J. Earth Sci.*, **49**, 661–695.

Cassidy, K.F., Champion, D.C., Krapez, B., Barley, M.E., Brown, S.J.A., Blewett, R.S., Groenewald, P.B. & Tyler, I.M., 2006. A revised geological framework for the Yilgarn Craton, Western Australia, *GSWA Record*, 1–8.

Cawood, P.A. & Tyler, I.M., 2004. Assembling and reactivating the Proterozoic Capricorn Orogen: lithotectonic elements, orogenies, and significance, *Precambrian Res.*, **128**, 201–218.

Clark, D. & Leonard, M., 2003. Principle stress orientations from multiple focal-plane solutions: new insight into Australian intraplate stress field, *Spec. Publ. Geol. Soc. Aust.*, **22**, 91–105.

Clitheroe, G., Gudmundsson, O. & Kennett, B.L.N., 2000. The crustal thickness of Australia, *J. geophys. Res.*, **105**(13), 13 697–13 713.

Coblentz, D.D., Zhou, S., Hillis, R.R., Richardson, R.M. & Sandiford, M., 1998. Topography, boundary forces, and the Indo-Australian intraplate stress field, *J. geophys. Res.*, **103**, 919–931.

Collins, C.D.N., Drummond, B.J. & Nicoll, M.G., 2003. Crustal thickness patterns in the Australian continent, *Geol. Soc. Am. Spec. Paper*, **372**, 121–128.

Diehl, T. & Kissling, E., 2007. *Users guide for consistent phase picking at local to regional scales*, ETH Zurich, Switzerland.

Dreger, D.S. & Helmberger, D.V., 1993. Determination of source parameters at regional distances with three-component sparse network data, *J. geophys. Res.*, **98**, 8107–8125.

Drummond, B.J., 1988. A review of crust/upper mantle structure in the Precambrian areas of Australia, *Precambrian Res.*, **40/41**, 101–116.

Du, Z.J. & Foulger G. R., 1999. The crustal structure beneath the northwest fjords, Iceland, from receiver functions and surface waves, *Geophys. J. Int.*, **139**, 419–432.

Fitzsimons, I.C.W., 2003. Proterozoic basement provinces of southern and southwestern Australia, and their correlation with Antarctica, *Geol. Soc. Lond. Spec. Pub.*, **206**, 93–130.

- Hardebeck, J.L. & Shearer, P.M., 2003. Using S/P amplitude ratios to constrain the focal mechanisms of small earthquakes, *Bull. seism. Soc. Am.*, **93**, 2434–2444.
- Herrmann, R.B., 2004. Computer programs in seismology, Version 3.30.
- Hickman, A.H., 2004. Two contrasting granite-greenstone terranes in the Pilbara Craton, Australia: evidence for vertical and horizontal tectonic regimes prior to 2900 Ma, *Precambrian Res.*, **131**, 153–172.
- Ivanic, T.J., Wingate, M.T.D., Kirkland, C.L., Van Kranendonk, M.J. & Wyche, S., 2010. Age and significance of voluminous mafic-ultramafic magmatic events in the Murchison Domain, Yilgarn Craton, *Aust. J. Earth Sci.*, **57**, 597–614.
- Julia, J., Ammon, C.J., Herrmann, R.B. & Correig, A.M., 2000. Joint inversion of receiver function and surface wave dispersion observations, *Geophys. J. Int.*, **143**, 99–112.
- Julia, J., Ammon, C.J. & Herrmann, R.B., 2003. Lithospheric structure of the Arabian Shield from the joint inversion of receiver functions and surface-wave group velocities, *Tectonophysics*, **37**, 1–21.
- Julian, B. & Foulger, G.R., 1996. Earthquake mechanisms from linear-programming inversion of seismic-wave amplitude ratios, *Bull. seism. Soc. Am.*, **86**, 972–980.
- Julian, B., Miller, A.D. & Foulger, G.R., 1997. Non-double-couple earthquake mechanism at the Hengill-Grensdalur volcanic complex, southwest Iceland, *Geophys. Res. Lett.*, **24**, 743–746.
- Kagan, Y.Y., 1992. Correlations of earthquake focal mechanisms, *Geophys. J. Int.*, **110**, 305–320.
- Kennett, B.L.N., Engdahl, E.R. & Buland, R., 1995. Travel times for global earthquake location and phase association, *Geophys. J. Int.*, **122**, 108–124.
- Kilb, D. & Hardebeck, J.L., 2006. Fault parameter constraints using relocated earthquakes: a validation of first-motion focal-mechanism data, *Bull. seism. Soc. Am.*, **96**, 1140–1158.
- Knopoff, L., Muller, S. & Pilant, W.L., 1966. Structure of the crust and upper mantle in the Alps from the phase velocity of Rayleigh waves, *Bull. seism. Soc. Am.*, **56**, 1009–1044.
- Langston C.A., 1979. Structure under Mount Rainier, Washington, inferred from teleseismic body waves, *J. geophys. Res.*, **84**, 4749–4762.
- Larsen, S.C. & Schultz, C.A., 1992. *E3D: 2D/3D Elastic Finite-Difference Wave Propagation Code*, Lawrence Livermore National Laboratory, 1–18.
- Levshin, A.L. & Ritzwoller, M.H., 2001. Automated detection, extraction, and measurement of regional surface waves, *Pure appl. Geophys.*, **158**, 1531–1545.
- Ligorria, J.P. & Ammon, C.J., 1999. Iterative Deconvolution and receiver-function estimation, *Bull. seism. Soc. Am.*, **89**, 1395–1400.
- Lobkis, O.I. & Weaver, R.L., 2001. On the emergence of the Green's function in the correlations of a diffuse field, *J. Acoust. Soc. Am.*, **110**, doi:10.1121/1.1417528.
- McCue, K., 1990. Australia's large earthquakes and recent fault scarps, *J. Struct. Geol.*, **12**, 761–766.
- Myers, J.S., 1993. Precambrian history of the West Australian craton and adjacent orogens, *Annu. Rev. Earth Planet. Sci.*, **21**, 453–485.
- Myers, J.S., Shaw, R.D. & Tyler, I.A., 1996. Tectonic evolution of Proterozoic Australia, *Tectonics*, **15**, 1431–1446.
- Özalaybey, S., Savage, M.K., Sheehan, A.F., Louie, J.N. & Brune, J.N., 1997. Shear-wave velocity structure in the northern Basin and Range province from the combined analysis of receiver functions and surface waves, *Bull. seism. Soc. Am.*, **87**, 183–199.
- Pasyanos, M.E., Dreger, D.S. & Romanowicz, B., 1996. Towards real-time determination of regional moment tensor, *Bull. seism. Soc. Am.*, **86**, 1255–1269.
- Rawlinson, N. & Sambridge, M., 2004a. Wavefront evolution in strongly heterogeneous layered media using the fast marching method, *Geophys. J. Int.*, **156**, 631–647.
- Rawlinson, N. & Sambridge, M., 2004b. Multiple reflection and transmission phases in complex layered media using a multistage fast marching method, *Geophysics*, **69**, 1338–1350.
- Reading, A.M. & Kennett, B.L.N., 2003. Lithospheric structure of the Pilbara Craton, Capricorn Orogen and northern Yilgarn Craton, Western Australia from teleseismic receiver functions, *Aust. J. Earth Sci.*, **50**, 439–445.
- Reading, A.M., Tkalčić, H., Kennett, B.L.N., Johnson, S.P. & Sheppard, S., 2011. Seismic structure of the crust and uppermost mantle of the Capricorn and Paterson orogens and adjacent cratons, Western Australia, from passive seismic transects, *Precambrian Res.*, doi:10.1016/j.precamres.2011.07.001, in press.
- Reasenber, P.A. & Oppenheimer, D.H., 1985. PPFIT, FPLOT and FPAGE: Fortran computer programs for calculating and displaying earthquake fault-plane solutions, *US Geol. Surv. Open-File Rept.*, **85–739**, 1–109.
- Revetts, S.A., Keep, M. & Kennett, B.L.N., 2009. NW Australian intraplate seismicity and stress regime, *J. geophys. Res.*, **114**, B10305, doi:10.1029/2008JB006152.
- Reynolds, S.D., Coblenz, D. D & Hillis, R.R., 2002. Tectonic forces controlling the regional intraplate stress field in continental Australia: Results from new finite element modeling, *J. geophys. Res.*, **107**(B7), 2131, doi:10.1029/2001JB000408.
- Reynolds, S.D., Coblenz, D.D & Hillis, R.R., 2003. Influences of plate-boundary forces on the regional intraplate stress field of continental Australia, *Geol. Soc. Am. Spec. Paper*, **372**, 59–70.
- Saikia, C.K., 1994. Modified frequency-wavenumber algorithm for regional seismograms using Filon's quadrature: modelling of Lg waves in eastern North America, *Geophys. J. Int.*, **118**, 142–158.
- Saygin, E. & Kennett, B.L.N., 2010. Ambient seismic noise tomography of Australian continent, *Tectonophysics*, **481**, 116–125.
- Šilený, J., Campus, P. & Panza G.F., 1996. Seismic moment tensor resolution by waveform inversion of few local noisy records—I. Synthetic tests, *Geophys. J. Int.*, **126**, 605–619.
- Sheppard, S., Johnson, S.P., Wingate, M.T.D. & Kirkland, C.L., 2010. The Paleoproterozoic Capricorn Orogeny: intracontinental reworking not continent-continent collision, *GSWA Record*, 2010/108, 1–33.
- Snoke, A., 2003. Focal mechanism determination software (FOCMEC package), <http://www.geol.vt.edu/outreach/vtso/focmec>.
- Spaggiari, C.V., Wartho, J. & Wilde, S.A., 2008. Proterozoic deformation in the northwest of the Archean Yilgarn Craton, Western Australia, *Precambrian Res.*, **162**, 354–384.
- Stein, S., 2007. Approaches to continental intraplate earthquake issues, *Geol. Soc. Am. Spec. Paper*, **425**, 1–16, doi:10.1130/2007.2425(01).
- Tkalčić, H., Pasyanos, M.E., Rodgers, A.J., Gök, R., Walter, W.R. & Al-Amri, A., 2006. A multistep approach for joint modeling of surface wave dispersion and teleseismic receiver functions: implications for lithospheric structure of the Arabian Peninsula, *J. geophys. Res.*, **111**, B11311, doi:10.1029/2005JB004130.
- Tkalčić, H., Dreger, D.S., Foulger, G.R. & Julian, B.R., 2009. The puzzle of the 1996 Bárðarbunga, Iceland, earthquake: no volumetric component in the source mechanism, *Bull. seism. Soc. Am.*, **99**, 3077–3085.
- Tkalčić, H., Chen, Y., Liu, R., Huang, Z., Sun, L. & Chan, W., 2011a. Multi-step modeling of teleseismic receiver functions combined with constraints from seismic tomography: crustal structure beneath southeast China, *Geophys. J. Int.*, **187**, 303–326, doi:10.1111/j.1365-246X.2011.05132.x.
- Tkalčić, H., Rawlinson N., Arroucau, P., Kumar, A. & Kennett, B.L.N., 2011b. Multi-Step modeling of receiver-based seismic and ambient noise data from WOMBAT array: crustal structure beneath southeast Australia, *Geophys. J. Int.*, submitted.
- Tyler, I.M. & Thorne, A.M., 1990. The northern margin of the Capricorn Orogen, Western Australia—an example of an early Proterozoic collision zone, *J. Struct. Geol.*, **12**, 685–701.
- Van Kranendonk, M.J., Smithies, R.H., Hickman, A.H. & Champion, D.C., 2007. Review: secular tectonic evolution of Archean continental crust: interplay between horizontal and vertical processes in the formation of the Pilbara Craton, Australia, *Terra Nova*, **19**, 1–38.
- Wellman, P., 2000. Upper crust of the Pilbara Craton, Australia; 3D geometry of a granite/greenstone terrain, *Precambrian Res.*, **104**, 175–186.
- Yao H., van der Hilst, R.D. & de Hoop, M.V., 2006. Surface-wave array tomography in SE Tibet from ambient seismic noise and two-station analysis. Part I. Phase velocity maps, *Geophys. J. Int.*, **166**, 732–744.
- Zhao, S. & Muller, R.D., 2003. Three-dimensional finite-element modelling of the tectonic stress field in continental Australia, *Geol. Soc. Am. Spec. Paper*, **372**, 71–89.